

Aerosol Jet Printing of Strain Sensors for Soft Robotics

Prakash Karipoth,* James H. Chandler, Jaemin Lee, Silvia Taccola, James Macdonald, Pietro Valdastrì, and Russell A. Harris

The field of soft robotics is rapidly progressing toward applications including; wearable electronics, prosthetics, and biomedical devices. This is leading to demand for flexible, embedded high-performance strain sensors to deliver real-time feedback on the static configurations and dynamic motions of these robotic devices, to ultimately enable the levels of autonomous control and structural monitoring required for intelligent manipulation. Herein, aerosol jet printing (AJP) technology is utilized to generate arbitrary piezoresistive strain sensor layouts on fibrous paper suitable for direct integration into elastomeric soft robots. A custom graphene nanoplatelet ink with a viscosity of around 2.70 cP has been formulated for optimized atomization and patterning of conductive traces via AJP. Single and multilayer printing onto different paper substrates are explored; with the nominal resistance of the printed tracks varying from 272 to 4900 k Ω depending on paper type and number of layers. Maximum gauge factors of 24.2 ± 1.8 and 56.5 ± 4.5 are determined for sensor surfaces under tensile and compression modes, respectively. To demonstrate the possibility for direct integration of this approach for soft robotics, strain sensors are directly printed onto the strain-limiting layer of a pneumatic soft robotic gripper, to provide continuous feedback of the gripper over curvatures up to 80 m^{-1} .

flexible and reliable strain sensors^[7] delivering continuous feedback for improved manipulation and control.^[8] Various types of strain sensors such as piezoresistive,^[9,10] capacitive,^[10,11] and optical^[12] have been reported, with the majority being fabricated using conventional manufacturing approaches such as casting,^[13] spray coating^[14] or multistep protocols,^[15] and requiring mounted via adhesive/mechanical bonding to the surface of the soft robot.^[16] This bonding approach can limit dimensional freedom and introduce discontinuity of elastic properties. It is therefore desirable to direct write sensors onto the body of the soft robot^[17] using digitally driven direct manufacturing techniques that can offer scalable, reproducible, and automated batch fabrication with reduced impact on the robot's performance.

Recently, there has been significant progress in digitally controlled fabrication of sensing devices using methods such as syringe-based extrusion 3D printing,^[18] digital light processing-based 3D print-

ing,^[19] and through utilization of biocompatible conductive polymer such as PEDOT:PSS.^[20] While most sensors fabricated using these approaches have shown appropriate performance, there has been limited exploration into their suitability for the direct writing of strain sensors onto soft robots. Amongst state-of-art direct write techniques, aerosol jet printing (AJP),^[21,22] which uses atomization of inks and dispersions to produce aerosol droplets which are transported and deposited using a carrier gas flow, has presented several unique advantages. These include contactless direct deposition with nozzle–substrate offsets in the range of 1–5 mm, scalability, miniaturization, and repeatability. Aerosol droplets, collimated and accelerated by a secondary annular gas flow (i.e., sheath gas), are focused through a nozzle to allow microfeature deposition and patterning onto a range of materials. Unlike conventional inkjet printing, AJP permits the use of a variety of materials and ink formulations with wide ranging viscosities (1–1000 cp) and allows for deposition on topologically complex and nonplanar rough surfaces.^[21]


Despite the maskless fabrication capability of AJP, there has been no significant exploration into its use for direct writing of strain sensors onto soft robots. Strain sensors reported using AJP appear limited in performance^[23] and are either incompatible or have not been explored for soft robotic applications.^[24] For example, Zhao et al.^[23] reported AJP strain sensors using silver tracks printed on precured carbon prepreg (preimpregnated) substrate.

1. Introduction

Over the last decade, the field of soft robotics has rapidly expanded bringing huge potential in mechanical flexibility,^[1] degrees of freedom,^[2] functionality^[3] and deployability,^[4] and overcoming some of the limitations of conventional robotics.^[5,6] The next generation of soft robots will benefit from highly

P. Karipoth, J. Lee, S. Taccola, J. Macdonald, R. A. Harris
Future Manufacturing Processes Research Group
School of Mechanical Engineering
University of Leeds
Leeds LS2 9JT, UK
E-mail: p.karipoth@leeds.ac.uk

J. H. Chandler, P. Valdastrì
Science and Technology of Robots in Medicine (STORM) Laboratory
School of Electronic and Electrical Engineering
University of Leeds
Leeds LS2 9JT, UK

 The ORCID identification number(s) for the author(s) of this article can be found under <https://doi.org/10.1002/adem.202301275>.

© 2023 The Authors. Advanced Engineering Materials published by Wiley-VCH GmbH. This is an open access article under the terms of the Creative Commons Attribution License, which permits use, distribution and reproduction in any medium, provided the original work is properly cited.

DOI: 10.1002/adem.202301275

The sensor was characterized up to 0.1% strain, yielding a low gauge factor (GF) of 2. There have been few reports on utilizing force/pressure sensors fabricated with AJP for possible soft robotic application. For instance, piezoresistive pressure sensing segments printed with silver nanoparticles on polyamide have been utilized for soft robotic application such as tactile fingertip sensors for smart gloves, providing a sensitivity of 1.35 kPa^{-1} in the pressure range of 5–600 kPa.^[25] Recently, organic electrochemical transistor-based force sensor with unilateral microriblets array design has been fabricated on polydimethylsiloxane (PDMS) using AJP and demonstrated pressure sensing performance with a sensitivity of 1.45 kPa^{-1} in the range of 0–50 kPa.^[26] However, for intended soft robotic applications, these sensors still require adhesive or mechanical attachment to the soft robot for integration.

To realize direct writing of sensors on soft robots via AJP, challenges relating to ink formulation, particle size limits, solvent volatility, and postprocessing requirements need to be addressed.^[21,27] Piezoresistive strain sensors have previously been fabricated on various substrates using conductive materials such as carbon black,^[28] graphite,^[29] graphene,^[30] Ag nanostructures,^[31] PEDOT:PSS,^[32] and eutectic gallium indium liquid metals.^[33] To be processable, AJP requires uniform ink suspensions with a viscosity compatible with atomization as well as optimum solvent volatility^[21] to avoid drying of the ink particles before they are deposited.^[22] AJP is also subject to characteristic particle size range^[21] of 0–50 and 0–500 nm for ultrasonic and pneumatic atomization, respectively.

With suitable materials formulation, AJP allows printing onto rough and porous surfaces such as paper. Among various substrates explored for flexible and printed devices, paper, owing to the presence of a constituent mesh like microscopic cellulose fiber network,^[34,35] has demonstrated broad potential^[5,36,37] with optimum mechanical strength under tensile strain^[34] in soft robotics,^[38] origami^[39] structures, disposable sensors,^[40] and wearable^[41] technology while offering a recyclable, lightweight, and sustainable^[42] alternative to plastic electronics.^[43] Coating paper with conductive nanomaterials has been demonstrated to generate resistive fiber networks which facilitate strain sensing behavior.^[37,42] The structural properties of paper have further allowed its use as a mechanically deformable backbone^[44,45] in soft robotics; with materials such as silicone elastomers,^[46] polypropylene,^[47,48] as a functional composite strain limiting layer,^[38] or to realize hybrid functionality such as bilayer actuators.^[48,49] Chen et al.^[35] studied the AJP of silver nanoparticle ink on cellulose paper, demonstrating the simplification of sintering requirements through the use of paper substrates for AJP. The AJP action facilitates the guided diffusion and capillary absorption of ink droplets toward the intra- and interfiber pores of paper.^[35] However, the potential for piezoresistive sensors printed on paper by AJP has not previously been explored for soft robotics.

In this work, we present a custom formulated graphene nanoplatelet (GNP) ink optimized to meet the requirements of AJP onto paper substrates for direct writing of sensors onto soft robots. The presented GNP formulation was selected for its high sensitivity with respect to other carbon counterparts^[50] and can be processed for AJP at room temperature. Through solvent selection, the requirements for postsintering processes of printed resistive tracks were removed, allowing for the direct

printing of paper-based sensors. We evaluate sensor performance variability due to substrate selection and for single-layer versus multilayer patterning, and demonstrate AJP-based direct writing of strain sensors on paper preintegrated in the silicone elastomer body of a pneumatic 4-finger soft grasper for the continuous and reliable strain sensing of the soft robotic actuation.

2. Results and Discussion

The tailored ink for AJP was custom formulated using GNP as conductive particles, ethyl cellulose (EC) as binder, and ethanol and terpineol as cosolvents. The custom ink was deposited via AJP onto various paper substrates for strain sensor development, as illustrated in **Figure 1**. The nature of the cellulose fiber network within paper impacts the texture, porosity, wettability, moisture retention, and mechanical strength, and its characteristics can also influence the quality and performance of the printed conductive tracks. Standard commercially available fibrillar paper types were utilized as substrates for printing of the formulated GNP conductive ink, including laboratory filter paper (Fisherbrand, pore size of 5–13 μm), weighing paper (Fisherbrand), and slip note paper (repositionable paper) (3 M, Post-it). These representative paper substrates were selected due to their low cost, wide availability, commercial standardized material quality, and the presence of microfibrillar features. The substrates are subsequently referred to as F-paper, W-paper, and S-paper, respectively.

2.1. Ink Characterization and AJP

The printable homogenous suspension of the custom formulated GNP ink is shown in **Figure 1a**. Sonication of the ink in ethanol for several hours during the ink preparation allows the segregation, aided by the EC binder, and dispersion of the GNP aggregates.^[21,51] The ink viscosity was determined before and after adding 10% by volume of terpineol in ethanol, and was found to be 1.78 and 2.70 cP, respectively. The increase in ink viscosity with terpineol addition can be attributed to the difference in kinematic viscosity of ethanol (1.10 cP at 25 °C) and that of terpineol (32.30 cP at 25 °C).^[52] The optimized viscosity lies well within the accepted range of 0.5–1000 cP specified for both ultrasonic (0.5–10 cp) and pneumatic atomization (0.5–1000 cp) in a typical AJP process.^[21,53,54] To overcome the challenge of delivering desired volatility while maintaining run-time stability, a cosolvent approach was employed with an optimized proportion of lower and higher volatility solvents, ensuring more consistency and reliability in the aerosol flow rate. Here, 10% by volume of terpineol (boiling point: 219 °C) to ethanol (boiling point: 78.37 °C) was selected to achieve solvent evaporation at an optimum rate during the printing process.

In-house^[55,56] AJP equipment configured with a bespoke multi-axis stage is used for the deposition of the ink. The details of the deposition arrangements and parameters are provided in the experimental section. A simplified schematic representation of the AJP technique is represented in **Figure 1b**. Atomized ink particles, suspended in carrier gas (e.g., N_2 gas), are guided to the nozzle for the final patterned deposition within a region of interest. Pneumatic atomization was selected due to its compatibility

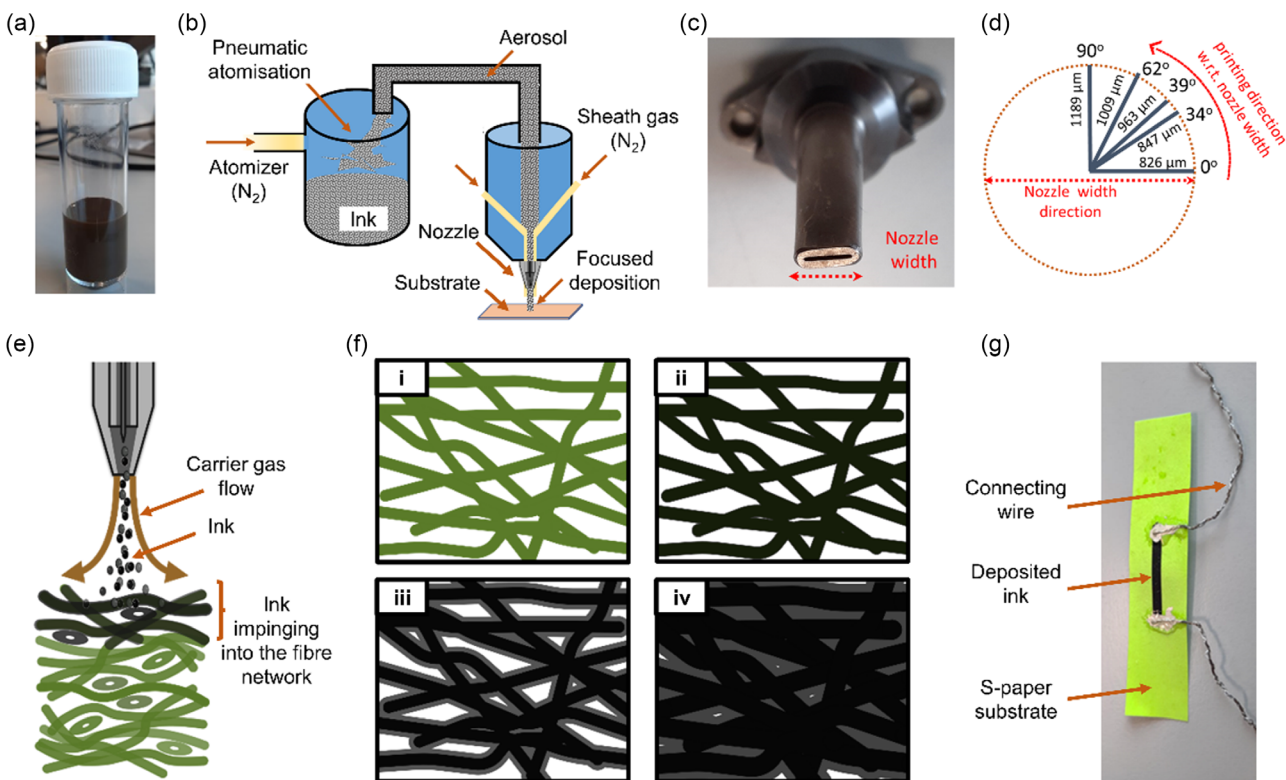


Figure 1. a) The formulated GNP ink; b) schematic of the AJP system; c) slot deposition nozzle; d) variation of track width with printing direction; e) schematic of ink deposition on paper fibers (cross-sectional view); f) stages of ink interaction with paper (representing a microscopic top view), showing (i) fibers with no ink deposition, (ii) individual fiber coating with single layer deposition, (iii) increased fiber coating thickness from successive deposition, and (iv) further depositions cover all voids forming a continuous graphitic layer; subsequent depositions act to increase the layer thickness g) a representative printed 20.0×1.5 mm sensor on S-paper.

with larger particle sizes, higher particle dispersibility, and printing nozzle and parameter selection when compared to ultrasonic atomization.^[56] A slot nozzle of dimensions ($1.25 \text{ mm} \times 0.25 \text{ mm}$) was used for printing (Figure 1c) to maximize track width and yield better gauge stability, electrical percolation, and conductivity. Printing speed and number of overlaying layers were also varied for the optimized fabrication of strain sensor on paper. Samples with n consecutive layers printed on S-, F-, and W-paper substrates are represented as Sn, Fn, and Wn, respectively.

The printing speed was varied from 0.25 to 5 mm s^{-1} in discrete intervals and the optical micrographs of the obtained single layer printed tracks on filter paper (F-paper) are provided in Figure S1, Supporting Information. Based on the analysis of these micrographs, 0.5 mm s^{-1} was selected as the optimal printing speed to achieve a continuous network of conductive GNP. To examine the influence on printed track width for varied slot nozzle direction, straight line tracks of equal length were printed on F-paper with a common origin XY coordinate and nozzle path varying in different directions (angles) with respect to the nozzle width (Figure 1d); all other parameters were held constant. Printing in parallel (0°) and perpendicular (90°) directions with respect to the nozzle width produced the minimum and maximum mean resultant track widths of 826 and $1189 \mu\text{m}$, respectively. For print directions between 0° and 90° , the track width varies between these values. To mitigate influence of this

parameter on printed sensor performance, all subsequent tracks were printed in a direction perpendicular to the width of the wide nozzle and parallel to the length of the substrate.

During the AJP of solvent-based inks on paper, the aerosol jet impinges on the surface of the paper, and apart from the ink particles being deposited on the paper fibers at the paper surface, the carrier gas and sheath gas are capable of diffusing the ink to be directed deeper into the underlying fiber network (Figure 1e). Thus, the particles may be deposited at a greater depths from the paper surface.^[35] For example, penetration of conductive ink of the order of 24.9 – $51.0 \mu\text{m}$ has been observed in AJP tracks on cellulose substrates such as paper or cardboard.^[57] During AJP of the GNP ink, in the cosolvent^[21] ink formulation, the ethanol, being a low volatile solvent, evaporates after surface impact. A proportion of the terpineol evaporates during its trajectory while the remaining smaller amount of terpineol reaches the substrate and either spreads out or evaporates over time. During initial single layer deposition, the individual fibers are coated with GNP. With successive deposition, the voids between fibers are also covered to form a continuous graphitic layer on the substrate. Subsequent depositions act only to increase the printed layer thickness. Illustration of these different stages of ink interaction with microscopic fibers in the paper is shown from a top view in Figure 1f(i–iv). The stages of ink droplets adhering to the paper substrate are similar to those in a typical inkjet printing process

on paper.^[58] Figure 1g shows a representative sample with a printed GNP ink track (S-paper). Electrical contacts were fixed at both ends of the track using a conductive silver paste (Electrolube) and reinforced with epoxy resin adhesive to complete the paper strain sensor.

2.2. Microscopic Analysis of Printed Tracks on Fibrous Papers

The microscopic properties of deposited conductive nanomaterials have a significant impact on electrical performance; these factors involve the distribution of the particles and the interaction between the particles and substrates. Under the chosen printing parameters, the deposition provided uniform deposition throughout the printed tracks across all paper substrates. To characterize the microscopic features of the printed tracks, optical micrographs were recorded at magnifications ranging from $5\times$ to $50\times$. The bare paper substrates for S-paper (a,b)(i), F-paper (c,d)(i), and W-paper (e,f)(i) are shown at two different magnifications for better comparison with the deposited tracks. **Figure 2a(ii–iv),b(ii–iv)** shows the optical micrographs of GNP ink printed on S-paper as a single layer and as an overlay of ten successive layers, respectively. As shown in Figure 2a(ii), the GNP ink is deposited as a uniform layer with well-defined edges and a nominal track width of $1778\ \mu\text{m}$. There are no visible crack formations, revealing that the GNP forms a thin, even distribution over the cellulose fibers. As the aerosol jet impinges on the paper surface, the ink penetrates into the fibrous layers of the paper, as observed in Figure 2a(iii). This is consistent with similar distribution of silver ink particles deposited on cellulose paper reported in the literature.^[35] The fine coating of the conductive graphitic particles on the interconnected cellulose fibers realizes a 3D resistive network,^[35] as depicted in Figure 2a(iv), which illustrates example pathways R1, R2, R3 with different resistance values depending upon their length, the density of the conductive coating, and tension of each fiber during its mechanical deformation. The inset shows the bare paper with crosslinked fibers forming a network which when uniformly deposited with the GNP ink leads to the formation of resistive fiber network. The equivalent resistance at any instance between any two nodes of the coated fiber network would be the equivalent combined resistance of all other fibers relevant to the specific network between the nodes in consideration. As compared to single layer, deposition of ten consecutive layers on S-paper results in the formation of microcracks (Figure 2b(ii)). With successive layers deposited, the GNP coating on the fibers grows in thickness, and gradually covers the microscopic voids between the fiber network. Thus, a continuous distribution of the graphitic layer is established bridging the gap between the fibers on the paper surface. Successive ink particles no longer wick to the core of the fibrous network and mostly deposit on the preceding layer as shown in Figure 2b(iii). The formation of cracks in ink-deposited particulate material tracks may be attributed to the evaporation of the solvent and drying induced shrinkage^[59] of the binder and particles. This solvent evaporation and particulate shrinkage creates fractals (islands) separated by microscopic voids forming cracks. The likelihood of increased crack formation in printed tracks will depend on multiple parameters such as nature of the substrate (mechanical and surface properties), the binder

properties, thermal treatment, printed material and ink solvent properties, quality and thickness of the printed deposition. In our case of printed GNP tracks on paper, the formation of cracks may be triggered by a combination of solvent wetting followed by evaporation,^[60] mechanical stress between the connected fibers and the void spaces between them, rearrangement and shrinkage of EC binder/printed nanostructures accompanied by layer spacing collapse and disintegration.^[61] Nucleation of cracks, in turn, accelerates the solvent evaporation and drying as more surface area is available for evaporation from regions exposed by the cracks.^[62] As previously reported, cracking also depends on the amount of deposited materials, being extensive for multilayer deposited tracks^[63] where the print thickness exceeds a critical cracking thickness (CCT).^[64] The cracking of the printed patterns and fractal formation is typically higher for a larger number of printed layers, as the volumetric shrinkage increases and the solvent evaporation from unit surface area is larger. In such cases, the thickness of deposition exceeds the CCT. This is also observed in our experiments (see Figure S2, Supporting Information) where cracking is more evident and significant with an increased number of printed layers. For single layer of deposition, the ink mostly coats the microscopic fibers while the voids between the fibers are retained. When additional layers are deposited, these voids are also filled by the GNP particles. Subsequent application of mechanical stress to the results in different strains within the fiber region and void regions which may further accelerate crack formation. Mitigation of crack formation may be possible through choice of substrates, binder, solvent, and particle properties, limiting the deposition thickness below the CCT, and by optimizing deposition processing, solvent evaporation, and sample drying parameters. Figure 2b(iii) provides a more clear view of the cracks which are a few microns wide. The formation of these cracks can be beneficial for realizing crack-based piezoresistive strain sensors,^[65–67] with slit geometry cracks subject to disconnection–reconnection under mechanical deformation facilitating a proportional change in electrical resistance with strain.^[67] Figure 2b(iv) shows the magnified micrograph of the uncoated fibers in the vicinity of the edge of printed tracks. After ten consecutive layers printed, the undesirable overspray^[21,68] common in AJP is minimal, as evident from the limited spots where the black GNP particles have been deposited outside of the main print area.

Figure 2c(ii–iv),d(ii–iv) shows optical micrographs of GNP ink printed on F-paper as a single layer and as ten consecutive layers, respectively. As shown in Figure 2c(ii), the GNP ink is deposited as a uniform track without any visible cracks by printing one layer. The edges are slightly more uneven than the single-layer deposition on S-paper considering the highly solvent absorptive nature of the filter paper. Figure 2c(iii) shows a magnified view of the F-paper fibers evenly coated with GNP particles, not only at the paper surface, but also on the inner fiber network. The inset shows a single fiber fully covered with the GNP particles adhered due to the presence of the EC binder in the ink. Filter papers are featured with a dense network of constituent fibers, as shown in Figure 2c(iv). The coating of graphitic particles on this connected network of fibers can act as a network of resistors similar to Figure 2a(iv). When the GNP ink is deposited as ten consecutive layers on the filter paper, they form a thick continuous conductive layer over the paper surface as shown in Figure 2d(ii), concealing the voids between the fiber network. Even though

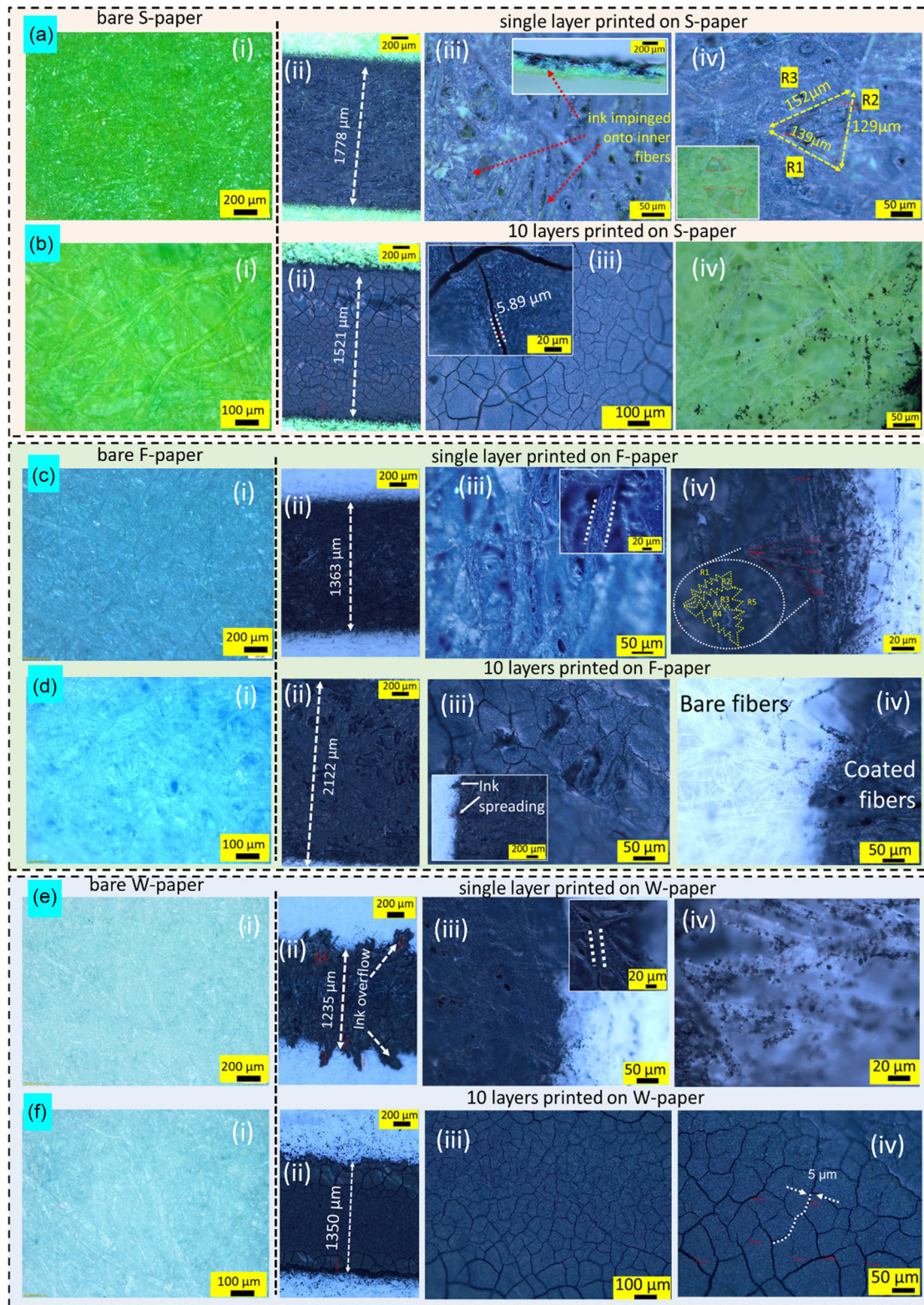


Figure 2. Optical microscope analysis of a,b) (i) bare S-paper; c,d) (i) bare F-paper; e,f) (i) bare W-paper at two different magnifications. Printed GNP samples on (a) (ii–iv) one layer on S-paper; (b) (ii–iv) ten layers on S-paper; (c) (ii–iv) one layer on F-paper (d) (ii–iv); ten layers on F-paper; (e) (ii–iv) one layer on W-paper; (f) (ii–iv) ten layers on W-paper.

cracks are visible, they are less prominent than for the S-paper (Figure 2b(ii)). This may be attributed to the nature of the fiber network, surface roughness, and faster absorption of solvent as compared to the S-paper. Laboratory filter papers typically have much higher wet strength, porosity, particle retention, and high-quality cellulose fibers as compared to other paper types. Figure 2d(iii) shows the magnified view of the cracks which are thin and uniform. As seen in the inset, when the ten overlaying tracks are printed continuously, there are minor spots of ink spreading when the solvent is not rapidly evaporated and instead gets infused and absorbed quickly by the filter paper along the edges of the printed track. Figure 2d(iv) shows the distinct fiber network of bare uncoated filter paper fibers as well as densely coated fibers with ten continuous layer depositions of GNP ink.

Figure 2e(ii–iv), f(ii–iv) shows the optical micrographs of GNP ink printed on W-paper as a single layer and overlay of ten consecutive layers, respectively. As shown in Figure 2e(ii), the single layer of GNP ink printed on the weighing paper yields less uniform tracks with uneven edges. This may be attributed to the higher wet resistant nature of the weighing paper as compared to the other two type of papers used. The printed region of the track is uniformly coated as evident from Figure 2e(iii). The inset shows uniformly coated individual fibers of the W-paper. Figure 2e(iv) shows more GNP particles deposited in the over-sprayed/ink-spread regions when compared to the S- and F-paper substrates. Figure 2f(ii) shows the ten consecutive overlapping layers of GNP tracks printed on the W-paper. Significant formation of cracks in the deposited track was observed as the solvent infusion and absorption were relatively low, resulting in the solvent molecules being retained on the surface until slowly evaporating away to form resulting cracks. The micrographs in Figure 2f(iii,iv) show the magnified view of random fractal formation by the cracks which are a few microns wide.

As observed in all samples in Figure 2, a slight variation in the printed track width for different paper substrates and different number of print layers was evident. The variation in width for different paper substrates is likely due to the paper surface

properties, wetting characteristics, pore size, and ink absorption properties. The variation may also be contributed by process drift, which is inherent in AJP techniques.^[54] Process drift mitigation strategies have been reported in literature, including ink recirculation,^[54] or real-time feedback with closed loop control of the printing process,^[69] however, these approaches were not employed as part of the presented system.

2.3. Electrical Characterization of Printed Tracks on Paper

The electrical resistance characteristics of the printed tracks on the paper substrates were measured using a precision digital multimeter (Keithley 2450 Sourcemeter). **Figure 3a** shows the resistance change of the GNP tracks according to the number of overlaying layers on paper. The initial single-layer resistance dramatically drops to 1/5th with the second layer which can be attributed to the low volume of the coated GNP particles limiting conductive pathways through the fiber network. As soon as the second layer is coated, the amount of the GNP particles, forming the conductive path, significantly increases, resulting in a thicker, denser film for higher conductivity. The resistance of the printed track decreases gradually with the increased number of layers and reaches a minimum of 272 k Ω at four layers. Over five layers of coating, the fibers are fully conductive but the ink does not penetrate as far into the inner fiber network; instead, the GNP particles now start to contribute to filling in the voids between the surface fiber network as discussed earlier and thus lower the overall electrical resistance. Similar saturation in the diffusion of particles toward subsurface fibers has been reported in the case of Ag particles printed on cellulose paper by AJP.^[35] Interestingly, further addition of layers did results in a slight increase in resistance, reaching 840 k Ω at ten layers as shown in Figure 3a. The appearance of cracks is the main source of the resistance increase due to the disconnected electrical paths which have been frequently observed in the literature.^[63,66] While comparing the variation in electrical resistance to the optical micrograph analysis of the printed tracks of varying

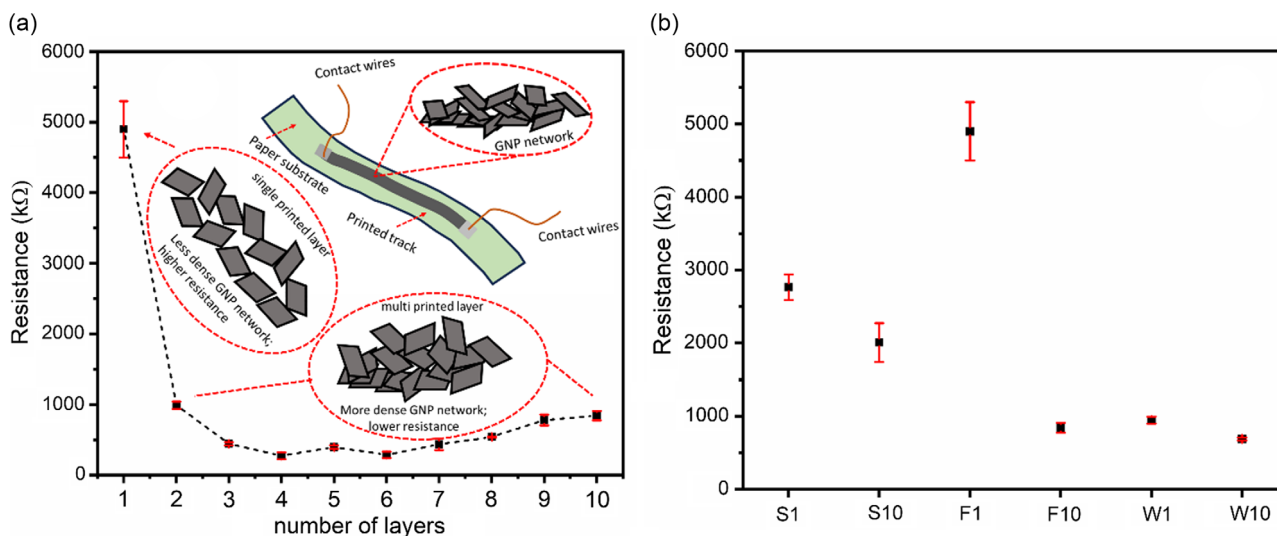


Figure 3. Variation of resistance of GNP ink printed on a) F-paper with varying number of printed layers; b) different types of paper with one or ten printed layers (error bar shown in red).

number of overlaying layers depicted in Figure S2, Supporting Information, it is observed that after four to five printed layers, microcracks start appearing. This is similar observation as in earlier reports^[70] on inkjet printed Ag tracks where larger cracks appear by more nonuniform solvent evaporation and larger gradient of solvent concentration with increasing deposition of layers and thereby layer thickness.

Figure 3b shows the variation of average resistance of GNP ink with single and ten consecutive layers printed on S, F, and W papers. In the case of S-paper, the resistance was around 2766 and 2006 k Ω for one and ten layers of deposition, respectively. Here, any favorable electrical enhancement in electrical conduction with more dense layers of GNP particle distribution is compromised by the formation of cracks and therefore no significant improvement in resistance is observed. In the case of filter paper (F), the high initial resistance of 4900 k Ω , originates from the microscopic pores in the filter paper fiber network which impede continuous film formation. In contrast to the S paper, a much lower resistance of 840 k Ω was obtained after ten-layer coating due to the dense and continuous conductive layer and comparatively lower crack formation and particle retention of the paper. W-paper showed a similar trend as S-paper and the resistance decreased from 946 to 686 k Ω after the layer accumulation.

2.4. Electromechanical Characterization of Printed Tracks as Strain Sensors

To investigate the electromechanical performance of printed GNP tracks on the paper substrates as piezoresistive strain

sensors, the S-, F-, and W-paper samples with one and ten layers of printing were subjected to cyclic bending performance characterization using a bespoke electro-mechanical system (Figure S3a, Supporting information) and image processing protocol (Figure S3b, Supporting Information), as described in the experimental section. Each sensor sample was clamped at either ends of the linear motor stage with the printed side facing upward and subjected to cyclic bending either upward (tensile, represented by u) or downward (compressive, represented by d) for 50 cycles. The instantaneous change in resistance was recorded using the digital multimeter and as a function of the bending strain $\epsilon = \kappa t/2$, where κ is the instantaneous curvature of the sample (+ve for upward bending), extracted via digital image analysis (Figure S3b, Supporting Information), and t the thickness of the paper substrate.

For comparison between samples, the relative resistance change and sensor strain for the final ten cycles of each test was considered. Figure 4a–c, respectively, shows the cyclic strain sensing response of the printed S-, W-, and F-paper strain sensors in compressive and tension modes.

For a given mechanical strain in bending ϵ , the performance of the strain sensor can be expressed in terms of relative change in resistance as $\Delta R/R_0$ (%), where R_0 is the original base resistance and R is the instantaneous resistance and $\Delta R = R - R_0$. ΔR is positive in the tensile mode and negative in the compressive mode as in the former case the conductive particles or network moves apart increasing the overall resistance whereas in the latter case, they come closer providing easier paths for conduction and thus lowering the effective resistance. As shown in Figure 4, all samples provided systematic cyclic response to the bending

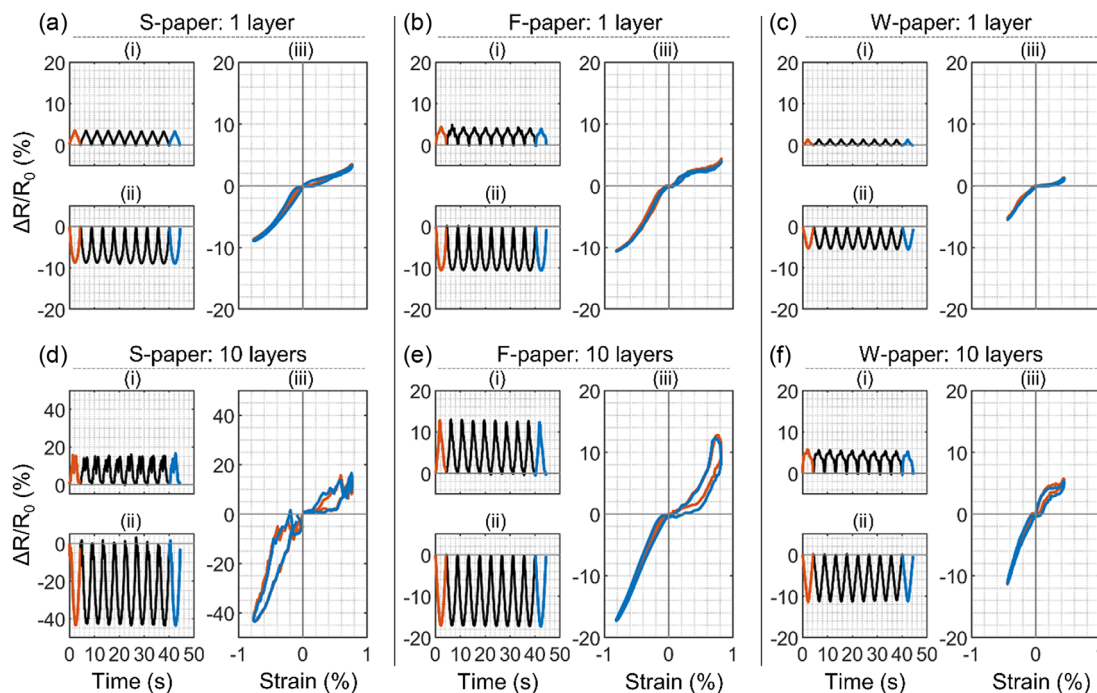


Figure 4. Cyclic bending characterization of printed GNP strain sensors as single layer on a) S-paper, b) F-paper, and c) W-paper and as ten layers on d) S-paper, e) F-paper, and f) W-paper. The subfigures (i) and (ii) denote the cyclic resistance change for tensile and compression modes of bending for each sample respectively, and (iii) denotes the corresponding hysteresis in both modes for the first (plotted in red) and last (plotted in blue) of the final ten test cycles.

deformation in both tensile and compressive modes. Figure 4a–c represents the bending response for single layer and (d–f) for ten layers printed on S-, F-, and W-paper, respectively. The subfigures (i) and (ii) denote the tensile and compression modes of bending for each sample and (iii) denotes the corresponding hysteresis in both modes. The S-, F-, and W-paper were subjected to a maximum bending strain of 0.77%, 0.82%, and 0.44%, respectively.

For the single layer of GNP ink printed, the maximum relative change in resistance in the tensile mode and compression mode was 3.5% and 8.7% for S-paper, 4.3% and 10.6% for F-paper, and 1.3% and 5.3% for W-paper, respectively. For single layer of GNPs, the piezoresistive strain sensing mechanism is based on the instantaneous mechanical strain of the cellulose fibers and the corresponding proportional change in resistance during deformation. Compared to S-paper, the slightly higher relative change in resistance for F-paper may be due to the characteristic dense fiber network for the filter paper. For W-paper, the response is comparatively less in both modes (tensile and compression) which could be likely due to the GNP particles being primarily distributed on the fibers of the paper surface and less within the paper (see Figure 2e(ii)). For all samples with single layer printed, the difference in amplitude of $\Delta R/R_0$ in the two modes is moderate indicating that the strain sensing response is more dependent on the magnitude of bending and the extent to which the individual fibers in the conductive network are evenly coated than the mode of bending.

For the ten overlaying layers of GNP ink printed, the maximum relative change in resistance in the tensile mode and compression mode was 14.2% and 43.4% for S-paper, 12.8% and 17.1% for F-paper and, and 5.7% and 11.4% for W-paper, respectively. For all three paper substrate types, the piezoresistive response is enhanced with multiple printed layers due to the dense multilayer network conductive GNP particles. The formation, nature, and distribution of microcracks on the ten-layer printed tracks also modulate the resistance behavior. In the tensile mode, as the paper is mechanically deformed, the GNP fractals separated by the cracks reversibly spread out, decreasing the electrical percolation and thus increasing the resistance significantly. In compression mode, the GNP fractals become closer in proportion to bending, facilitating new and shorter conductive paths and thus reducing the resistance. This decrease in resistance mediated by crack closure is of higher contribution than that of the compression of fibers and hence an overall decrease in resistance of approximately 43% for S-paper is evident. The $\Delta R/R_0$ in the compression mode for ten layers on filter paper is comparatively less than that for the S-paper because of the less significant crack formation. For the W-paper substrate, the strain sensor performance is significantly lower due to the smooth surface texture which results in the GNP particles deposited more on the paper surface and reduced deposition in the inner network of the paper fiber network as compared to the other substrates. This is also substantiated from Figure 3b by the comparatively lower resistance in W-paper samples. For all samples with ten layers printed, the difference in amplitude of $\Delta R/R_0$ in the two modes is much enhanced as the resistance variation mechanism is mainly governed by the crack propagation and closure whereas crack formation is less evident for single GNP coating layer.

In addition to the relative resistance change magnitude, consideration of resistance hysteresis is critical to produce reliable strain sensors. Piezoresistive strain sensors are usually associated with nonzero hysteresis^[71] in their dynamic response to applied elastic strain and it is highly desirable to have as little hysteresis^[72] as possible for practical applications. The first (plotted in red) and last (plotted in blue) representative strain hysteresis during the cyclic loading and unloading of each of the samples is shown in the corresponding subfigures (iii) in Figure 4. The hysteresis is comparatively less for all the samples with single layer printed as evident from the narrow hysteresis loops. This suggests that once the loading is removed, the device restores its original microscopic configuration of conductive network providing reliable and repeatable performance. The hysteresis is more evident for samples printed with ten layers, as crack formation and propagation govern the sensing mechanism. After the loading cycle, due to the nature and orientation of the cracks, the original configuration of the conducting network would be restored, while the dynamics of electrical conductive paths during the unloading may be slightly different as that during the loading cycle. The hysteresis observed in all the samples is less and comparable to those reported in the literature.^[71,72]

The quality factor metric or sensitivity of piezoresistive strain sensor is usually expressed as GF obtained as

$$GF = \frac{\Delta R / R_0}{\epsilon} \quad (1)$$

Table 1 shows the GF of the strain sensors fabricated by AJP of GNP ink on different types of paper substrates. The GF has been calculated as the average slope of the relative resistance change versus strain plot. As evident from the relative change in resistance (Figure 4) with externally applied bending strain, the GF is higher in the compression mode as compared to the tension mode. Maximum GF obtained in the tensile and compressive modes was 56.5 ± 4.5 for and 24.2 ± 1.8 , respectively, for the S10 sample. The GF is comparable with some of the reported values in the literatures such as 7,^[73] 42,^[74] and 46.^[48]

To verify the suitability and reliability of the fabricated strain sensors for soft robotic applications, the cyclic response at different strain values and stability^[75] was evaluated for the different paper substrate samples (Figure 5). It was observed from cyclic testing and analysis (Figure 4) that the compressive mode exhibited better performance than tensile mode. This mode was thus considered exclusively for the subsequent cyclic and stability

Table 1. Calculated average (mean \pm SD) GF of the various samples tested.

Nos.	Sample	Gauge factor	
		Tensile mode	Compressive mode
1.	S1	4.1 \pm 0.1	11.5 \pm 0.3
2.	S10	24.2 \pm 1.8	56.5 \pm 4.5
3.	F1	4.7 \pm 0.2	14.2 \pm 0.4
4.	F10	17.6 \pm 1.2	22.8 \pm 0.3
5.	W1	3.1 \pm 0.3	12.9 \pm 0.4
6.	W10	9.1 \pm 0.9	27.2 \pm 0.7

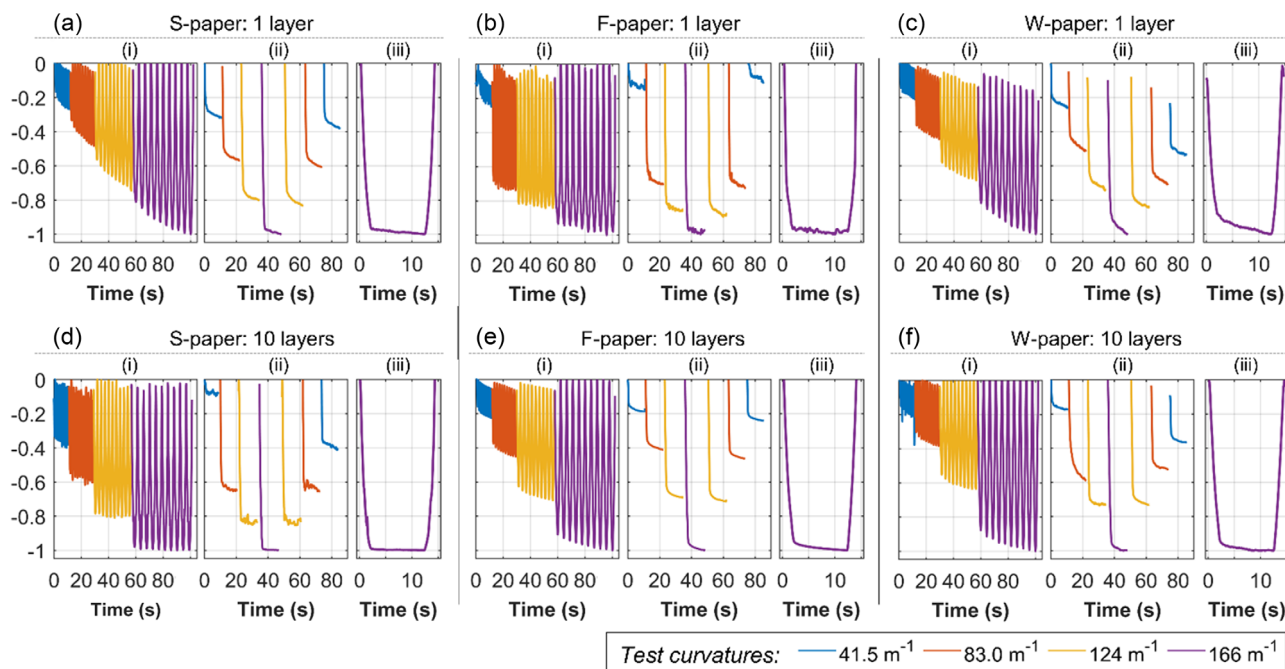


Figure 5. Varied compression mode testing for a) one-layer S-paper, b) one-layer F-paper, c) one-layer W-paper, d) ten-layer S-paper, e) ten-layer F-paper, and f) ten-layer W-paper. Results shown for (i) cyclic testing with ten cycles performed four increasing curvature values, (ii) quasistatic testing at stepped curvature values (increasing and decreasing) with each held for 10 s, and (iii) stability at maximum curvature over 10 s. Data on y-axis shown as the relative resistance change normalized to the resistance at maximum curvature.

testing for ease of comparison between the three sets of samples; data are presented as relative to resistance change at maximum curvature. Cyclic testing at varied curvatures shows evidence of drift in some samples, while other offer a more consistent response. This is also reflected in the stability testing over 10 s. Based on comparison across all samples, the most stable sensor performance in terms of cyclic and quasistatic testing was found to be the S-paper with ten print layers (Figure 5d).

Consequently, considering the paper-based strain sensor performance identified across the various electromechanical testing, it is hypothesized that these devices may be well suited for application as bending strain sensors within soft robotic applications, when careful selection of substrate and print layers is made. Subsequent evaluation to this end, therefore, considers the ten-layer S-paper sensor design as the most suitable candidate for direct integration into soft robotic designs.

2.5. Reinforcement of Conductive Tracks with Ecoflex Coating

As an important consideration for successful application within soft robot designs, sensor integration and robustness must be considered. Paper is generally fragile with poor tear resistance and sensitivity to moisture, dust, humidity,^[76] mechanical impact, and other environmental influences.^[77,78] Subsequently, it is beneficial to protect and electrically isolate the surface of the sensor through coating or encapsulation (Figure 5b).^[77] As soft robots are typically made with silicone elastomers, utilizing this material for sensor encapsulation would assist in its integration through better mechanical coupling to the body of the robot.

Therefore, a thin layer of Ecoflex was applied via spin coating over the printed side of a representative S10 samples.

The coated region is microscopically shown in Figure 6a where the printed GNP layer is still visible beneath the thin elastomer layer. As noted previously, strain sensor performance and stability for ten-layer sensors are governed by the cracks dynamics of the printed conductive tracks. The uncured prepolymer applied to the GNP printed surface partially infiltrated into the conductive networks and cracks similar to that reported in the literature^[79] where PDMS partially infiltrated into CNT papers during encapsulation. The infiltration of nonconductive Ecoflex also increases the effective base resistance (around 300% in our case) of the devices as the presence of infused elastomer across the printed GNP layer reduces the effective conductive paths in the network of the GNP particles. However, the sensing response is determined by the relative change in resistance during deformation and so these are still suitable for strain sensing applications. Figure 6c,d, respectively, shows the sensing response in tension mode and compression mode of the S10 sample with spin coated Ecoflex protective layer and without Ecoflex encapsulation. In the case of the uncoated sample, the sensor shows a cyclic response in response to the tensile and compressive deformations. However, the resistance variation shows random spikes. This is due to the fact that a fraction of the deposited particles may be loosely adhered to the substrate and, during deformation, instantaneous conductive paths may be formed and broken resulting in resistance spikes. Also, owing to the common hysteresis in piezoresistive materials, the configuration of the particle distribution would not be completely restored after each loading–unloading cycle. However, the characteristic strain

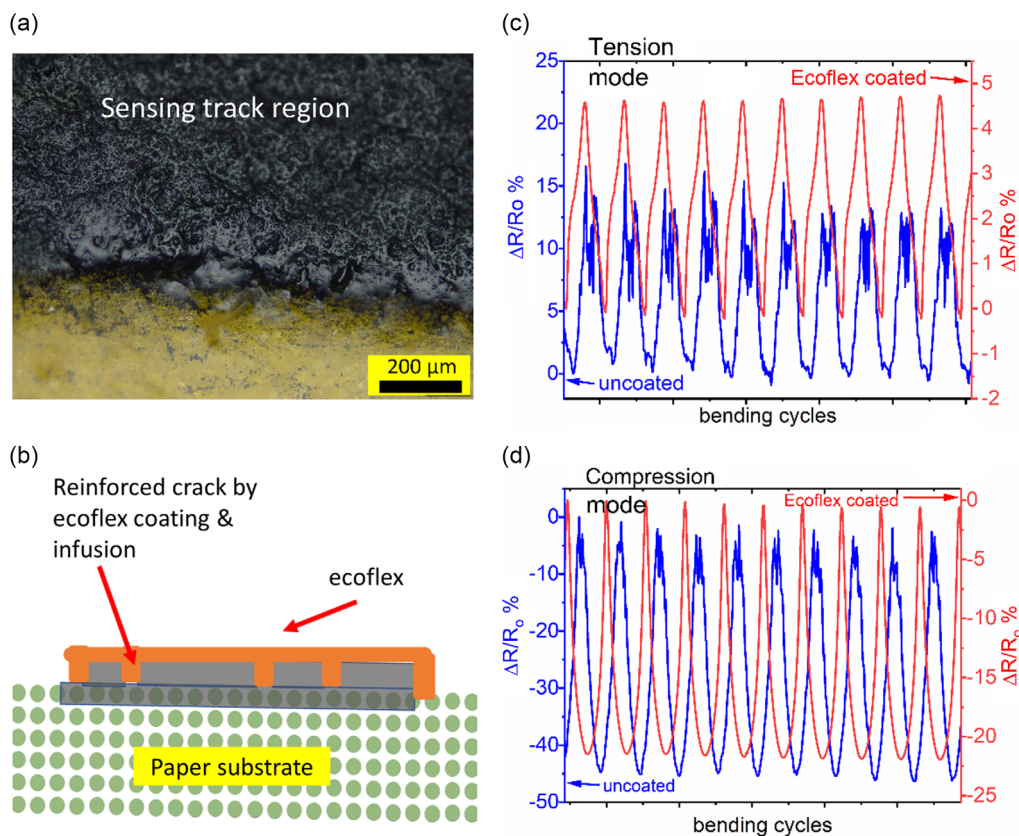


Figure 6. a) Optical micrograph of S10 sample with Ecoflex spin coated; b) schematic representation of the elastomer coating approach on paper strain sensor. Comparison of performance of S10 sample with and without Ecoflex coating in c) tension mode and d) compression mode.

sensing response to cyclic bending deformation of the samples after the Ecoflex coating is applied is maintained in both modes, and is comparatively more uniform and smooth. This may be attributed to the reinforcement of the printed track by the elastomer and its elastic nature facilitating restoration of the initial state of the sensing track after the deformation load is removed. Hence, the instantaneous conductive path formation during deformation may reorganize more systematically when an encapsulation layer is present as compared to uncoated counterparts. The improvement in stability of crack-based strain sensors with elastomer coating has also been validated in the literature.^[76] The relative change in resistance ($\Delta R/R_0$) for the Ecoflex-coated S10 samples in the tension and compression modes was obtained as around 4.7% and 21.5% as compared to 16.5% and 44.5% for the samples without Ecoflex coating. This reduction could be attributed to the increase in base resistance R_0 (so that $\Delta R/R_0$ would be lower for similar value of ΔR) with elastomer coating as well as the reinforcement of the conducting track by the elastomer.

Based on these discussions, it is evident the encapsulation of sensors with low water permeability and high chemical resistance polymers can enable water and corrosion resistance capabilities; this assures the durability and reliability of such sensors in soft robotics and wearables applications.^[77] Moreover, materials such as paper, fibers, and fabrics are known to be suitable for use as reinforcement structures or strain limiting layers^[45] which are fully embedded in soft robots. Embedding a strain sensing

capability in these materials can add proprioception and control functionality in soft robots, without the compromise of additional attachments such as surface mounted sensors which are prone to environmental influences.

2.6. Direct Writing of Strain Sensors on Soft Robots for Sensing and Feedback

As discussed in the introduction, independent fabrication of strain sensors and their integration with soft robots has its own practical difficulties and limitations. Hence, it is greatly advantageous if the strain sensors could be directly fabricated on the surface of a soft robot. AJP is well suited for this scenario as a maskless, direct writing technology enabling precise deposition of various inks on complex surfaces.

To explore the potential of our sensor manufacturing approach for soft robotic applications, we employed AJP of the custom GNP ink to directly write onto the strain limiting paper substrate of a soft pneumatic finger (**Figure 7a** and Video S1, Supporting Information). The details of gripper fabrication and sensing material deposition by AJP are provided in the Experimental Section. The design and printing flexibility in AJP allowed the creation of a U-shaped conductive track of 2 mm track width and 1 mm separation. From this, conductive electrodes could be attached at the center of the gripper and

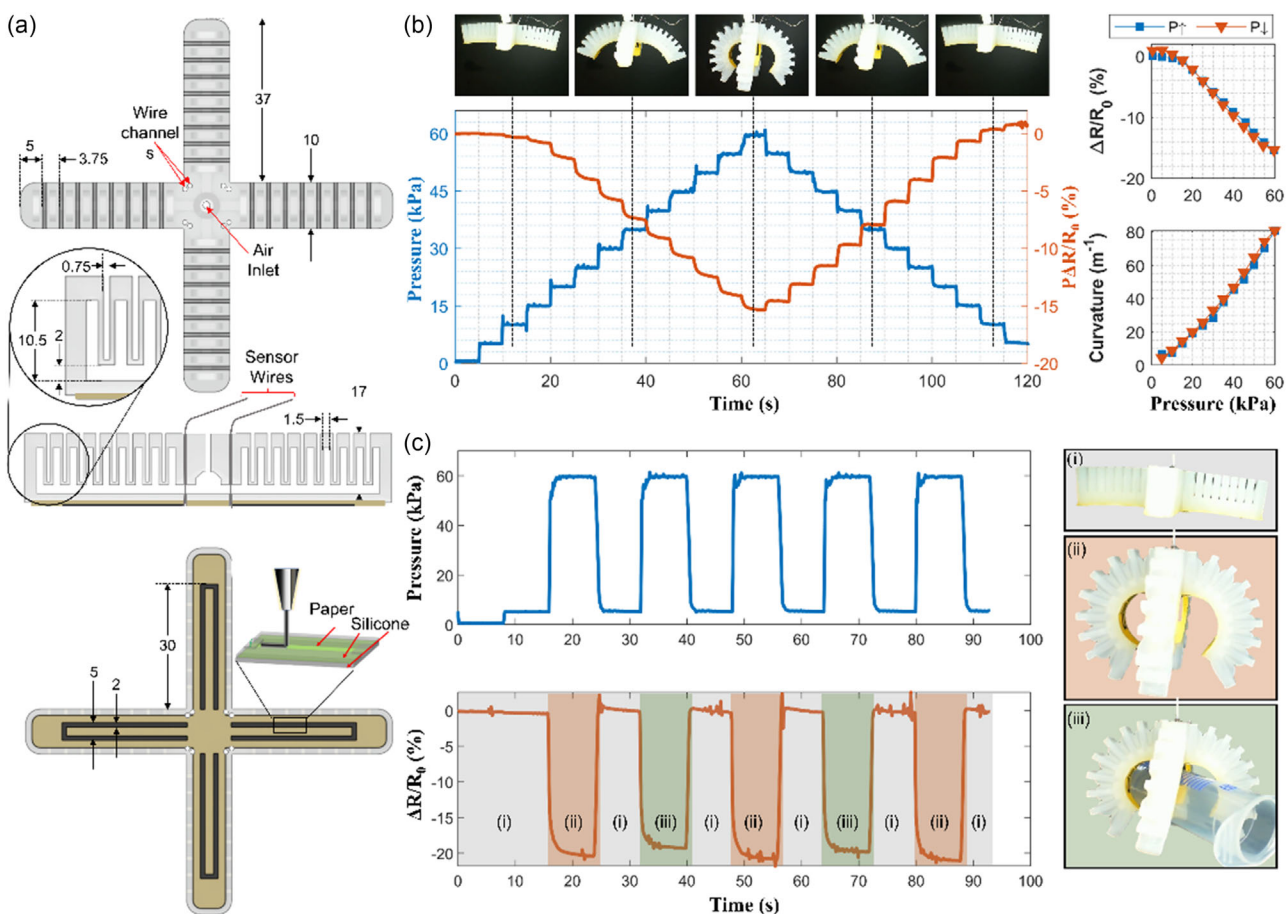


Figure 7. Soft robotic gripper with integrated AJP sensors for detection of arm curvature, showing a) the soft robotic gripper and strain limiting paper layer design and dimensions, including AJP GNP track geometry; b) sensor performance under pressure testing of the gripper, illustrating clear resistance change for pressure steps of 5 kPa and sensitivity across the range of pressures and arm curvatures; and c) relative resistance response of the integrated sensor with and without object grasp interactions.

sensor wires fed to proximal side and away from the grip surface for monitoring the resistance across the track. The sensing response of the gripper during its actuation with varying input pressure is shown in Figure 7b. The resistance response shows a clear relation to applied pressure, with distinct step changes evident from the 5 kPa pressure steps (Video S2, Supporting Information). This becomes more prominent as the pressure increases due to the high curvatures realized by the gripper arm. Furthermore, the response shows low noise and hysteresis for increasing and decreasing pressures, allowing precise tracking of the gripper curvature. For gripping tasks (Figure 7c), the reduced bending strain under object interaction results in lower resistance change for the same applied pressure (Video S3, Supporting Information). This demonstrates suitable sensitivity of the AJP sensor for repeatable detection of the object.

3. Conclusion

In this work, we have explored for the first time the potential of AJP as a maskless, direct writing technology to manufacture piezoresistive strain sensors on paper substrates for use in soft

robotic applications. For the strain sensing element, we formulated GNP ink using ethanol as primary solvent and terpineol as cosolvent for controllable evaporation. Three paper substrates were evaluated as candidates for the fabrication of strain sensors. The electrical and microscopic distribution of the conductive tracks were successfully controlled by the AJP parameters and the excellent electromechanical performance and reliability of the sensors were verified by analysis. The paper substrate was used as a strain limiting layer of a 4-finger pneumatic gripper and the sensor directly printed on the soft robotic device as a uniform track with predefined design. The pneumatic gripper was further characterized for its instantaneous strain response during actuation with and without object interaction. The combination of aerodynamically directed deposition of tailored ink and the characteristic cellulose fibrous architecture of paper as a substrate demonstrates new practical solutions toward strain sensor integration for soft robots overcoming the limitations of surface mounted or stick-on strain sensors. Future investigation of AJP for sensor integration into soft robots may also consider in-depth analysis of temperature dependence of resistance and using the presented approach to establish further capabilities such as slippage detection for robotic grasping stability.

Additionally, development of AJP inks and processes to allow direct printing onto the elastomeric material of the soft robot body would further expand the level of sensor integration possible.

4. Experimental Section

Ink Formulation: The GNP ink was formulated as follows: GNP (surface area: $500\text{ m}^2\text{ g}^{-1}$) aggregates, EC, ethanol, and terpineol were obtained from Fisher Scientific. Initially 0.8 g of EC was dissolved in 70 mL of ethanol. Following this, 2 g of GNP was added to the ethanol–EC solution and sonicated in a laboratory ultrasonic bath for 4 h. Further, terpineol was added at 10% by volume accompanied by magnetic stirring and further sonicated for better dispersion and uniformity.

Ink Viscosity Measurements: The viscosity of the GNP ink was determined to an accuracy of $\pm 2\%$ using a small sample viscometer (microVISC-m- Rheosense, Inc.).

AJP: The in-house AJP equipment configured with a bespoke multi axis stage and a computer controlled interface for the maskless directed deposition of the atomized ink on various substrates and surfaces was used for the deposition of the ink. The aerosol ink droplets generated by atomization were dispersed in a controlled flow of gas (nitrogen) and transported to a deposition nozzle head. Gas flow rates for the pneumatic atomization and deposition of the formulated GNP ink were 300 sccm (sheath gas flow rate), 200 (exhaust gas flow rate), and 250 sccm (atomization gas flow rate). The GNP ink was printed on the chosen paper substrates to produce conductive tracks as straight lines of desired lengths. The nozzle was maintained at a fixed offset height (3 mm) from the substrate while the tool path was controlled in the X–Y plane.

Optical and Electrical Measurements: The optical microscopic characterization of the samples was carried out with an Olympus BX53M. The electrical characterization of the sample was carried out using a Keithley 2450 Digital SourceMeter.

Electromechanical Characterization: The system comprises one fixed and one variable displacement clamp mount. Clamp displacement and velocity were controlled via a linear actuator (S20-50-38-B, Actuonix, Canada) and stepper driver board (uStepper S, uStepper, Denmark). Test samples were clamped at either end at a fixed clamp separation of 30 mm and positioned with the printed sensor region facing upward and slight precurvature to induce either upward (tensile) or downward (compressive) bending upon application of linear motion (see Figure S3, Supporting Information). For cyclic testing (Figure 4), 50 linear actuation cycles (10 mm peak-to-peak amplitude) were performed on each sample under each configuration while the printed sensor resistance was concurrently measured (2450 Digital SourceMeter, Keithley, USA) and the bending recorded via a camera (acA2040-120uc, Basler AG, Ahrensburg, Germany) positioned orthogonally to the bending plane. Subsequent image processing (Vision Development Module, National Instruments, USA) was used to extract the sample curvature as a function of cycle position (Figure S3b, Supporting Information). Based on the paper thickness, the associated strain on the printed sensor was calculated as $\epsilon = \kappa t/2$, where κ is the curvature of the sample (+ve for upward bending) and t is the thickness of the paper substrate. For cyclic and quasistatic stability testing at different curvature values (Figure 5), the same electromechanical test setup was used, with samples being tested over four different strain levels (corresponding to 25%, 50%, 75%, and 100% of maximum curvature), where maximum curvature was determined from peak linear displacement, in accordance with the cyclic testing. For cyclic testing at different curvatures, ten cycles were conducted at each curvature. For quasistatic tests, samples were driven over single cycles to each curvature value (increasing and decreasing) with a 10 s hold applied at each level. Resistance values were concurrently measured in all tests (2450 Digital SourceMeter, Keithley, USA).

Soft Robotic Gripper Fabrication: A soft robotic gripper was developed based on a standard fast Pnue-net design^[80] with four gripping fingers actuated simultaneously; dimensions presented in Figure 7a. A two-part mold was designed with the appropriate negative geometry of the gripper

to allow formation of the internal cavity features and external corrugations. A two-part silicone (Dragon Skin 10 Medium, Smooth-On, USA) was prepared in equal mass ratio and mixed under vacuum (ARV-310, THINKYMIXER, Japan) for 90 s at 1400 rpm and 20 kPa. The prepared mixture was injected into the open mold and placed inside a vacuum chamber for 120 s to remove any residual trapped air before being left to cure at room temperature for a minimum of 4 h. The open face of the cured part was then sealed by setting it into freshly prepared silicone of the same type poured into a shallow mold and allowing to cure at room temperature for a minimum of 4 h. Upon demolding, the strain-limiting paper layer was attached to the sealed side of the soft robotic gripper using a thin layer of the silicone. The completed gripper contains hollow channels to allow independent routing of sensor connection wires and a central air channel coupling the four arms (Figure 7a).

Printing onto the Gripper: The soft gripper was positioned into the AJP with the paper layer facing the print nozzle and aligned on the X–Y stage. The nozzle was maintained at a height of 3 mm from the paper layer surface. All other printing parameters and conditions are similar to that followed during the optimization of the strain sensor fabrication. Conductive GNP ink was printed on each arm of the gripper in a U-shaped pattern to allow connection to be made close to the center of the gripper. Connection wires were routed through the hollow channels and away from the gripping face.

Soft Robotic Gripper Demonstration: To test the soft robotic gripper, regulated air pressure was applied to introduce simultaneous bending of the gripper arms (Figure 7b). A pressure regulator (ITV001-3BL, SMC Corporation, Japan) was connected to the inlet of the gripper and controlled via a data acquisition card (USB-6211, National Instruments, USA) and associated software (LabVIEW, National Instruments, USA) to deliver a pressure range between 0 and 60 kPa in increasing followed by decreasing steps of 5 kPa. During testing, the resistance of the gripper arm under test was captured using a digital meter (2450 Digital SourceMeter, Keithley, USA) while a camera (acA2040-120uc, Basler AG, Ahrensburg, Germany) was positioned orthogonally to the arm under measurement and image analysis used to determine the curvature of the arm.

Supporting Information

Supporting Information is available from the Wiley Online Library or from the author.

Acknowledgements

P.K. and J.H.C. contributed equally to this work. Research reported in this article was supported by the Engineering and Physical Sciences Research Council under grant nos. EP/P027687/1 and EP/V009818/1.

Conflict of Interest

The authors declare no conflict of interest.

Data Availability Statement

The data that support the findings of this study are available from the corresponding author upon reasonable request.

Keywords

aerosol jet printing, direct writing, paper-based sensors, piezoresistive ink, soft robots, strain sensors

Received: August 14, 2023
Revised: October 13, 2023
Published online: November 15, 2023

- [1] C. Laschi, B. Mazzolai, M. Cianchetti, *Sci. Rob.* **2016**, *1*, aah3690.
- [2] J. Wang, A. Chortos, *Adv. Intell. Syst.* **2022**, *4*, 2100165.
- [3] Y. Dong, L. Wang, N. Xia, Z. Yang, C. Zhang, C. Pan, D. Jin, J. Zhang, C. Majidi, L. Zhang, *Sci. Adv.* **2022**, *8*, abn8932.
- [4] A. Sedal, A. H. Memar, T. Liu, Y. Mengüç, N. Corson, *IEEE Rob. Autom. Lett.* **2020**, *5*, 2272.
- [5] G. M. Whitesides, *Angew. Chem., Int. Ed.* **2018**, *57*, 4258.
- [6] a) E. W. Hawkes, C. Majidi, M. T. Tolley, *Sci. Rob.* **2021**, *6*, abg6049; b) C. Majidi, *Adv. Mater. Technol.* **2019**, *4*, 1800477.
- [7] a) H. Liu, Q. Li, S. Zhang, R. Yin, X. Liu, Y. He, K. Dai, C. Shan, J. Guo, C. Liu, *J. Mater. Chem. C* **2018**, *6*, 12121; b) O. A. Araromi, M. A. Graule, K. L. Dorsey, S. Castellanos, J. R. Foster, W.-H. Hsu, A. E. Passy, J. J. Vlassak, J. C. Weaver, C. J. Walsh, *Nature* **2020**, *587*, 219.
- [8] a) P. Karipoth, A. Christou, A. Pullanchiyodan, R. Dahiya, *Adv. Intell. Syst.* **2022**, *4*, 2100092; b) H. Wang, M. Totaro, L. Beccai, *Adv. Sci.* **2018**, *5*, 1800541; c) H. Soury, H. Banerjee, A. Jusufi, N. Radacsi, A. A. Stokes, I. Park, M. Sitti, M. Amjadi, *Adv. Intell. Syst.* **2020**, *2*, 2000039; d) B. Shih, C. Christianson, K. Gillespie, S. Lee, J. Mayeda, Z. Huo, M. T. Tolley, *Front. Rob. AI* **2019**, *6*, 30.
- [9] P. Karipoth, A. Pullanchiyodan, A. Christou, R. Dahiya, *ACS Appl. Mater. Interfaces* **2021**, *13*, 61610.
- [10] L. Duan, D. R. D'hooge, L. Cardon, *Prog. Mater. Sci.* **2020**, *114*, 100617.
- [11] S.-R. Kim, J.-H. Kim, J.-W. Park, *ACS Appl. Mater. Interfaces* **2017**, *9*, 26407.
- [12] a) J. Guo, B. Zhou, R. Zong, L. Pan, X. Li, X. Yu, C. Yang, L. Kong, Q. Dai, *ACS Appl. Mater. Interfaces* **2019**, *11*, 33589; b) A. Leber, B. Cholst, J. Sandt, N. Vogel, M. Kolle, *Adv. Funct. Mater.* **2019**, *29*, 1802629.
- [13] a) L. Zhang, F. Jiang, L. Wang, Y. Feng, D. Yu, T. Yang, M. Wu, M. Petru, *Appl. Compos. Mater.* **2022**, *29*, 1621; b) A. Georgopoulou, C. Kummerlöwe, F. Clemens, *Sensors* **2020**, *20*, 2399; c) Y. Zheng, Y. Li, K. Dai, Y. Wang, G. Zheng, C. Liu, C. Shen, *Compos. Sci. Technol.* **2018**, *156*, 276.
- [14] a) M. Hu, Y. Gao, Y. Jiang, H. Zeng, S. Zeng, M. Zhu, G. Xu, L. Sun, *Adv. Compos. Hybrid Mater.* **2021**, *4*, 514; b) P. Zhang, Y. Chen, Y. Li, Y. Zhang, J. Zhang, L. Huang, *Sensors* **2020**, *20*, 1154; c) S. J. Park, J. Kim, M. Chu, M. Khine, *Adv. Mater. Technol.* **2016**, *1*, 1600053.
- [15] Q. Liao, M. Mohr, X. Zhang, Z. Zhang, Y. Zhang, H.-J. Fecht, *Nanoscale* **2013**, *5*, 12350.
- [16] a) S. Otake, S. Konishi, presented at 2018 IEEE Micro Electro Mechanical Systems (MEMS), Belfast, Ireland 21–25 January, **2018**; b) T. Yamada, Y. Hayamizu, Y. Yamamoto, Y. Yomogida, A. Izadi-Najafabadi, D. N. Futaba, K. Hata, *Nat. Nanotechnol.* **2011**, *6*, 296.
- [17] S. Y. Kim, Y. Choo, R. A. Bilodeau, M. C. Yuen, G. Kaufman, D. S. Shah, C. O. Osuji, R. Kramer-Bottiglio, *Sci. Rob.* **2020**, *5*, aay3604.
- [18] Y. Song, L. Chen, Q. Yang, G. Liu, Q. Yu, X. Xie, C. Chen, J. Liu, G. Chao, X. Chen, *ACS Appl. Nano Mater.* **2023**, *6*, 8937.
- [19] X. Xiong, Y. Chen, Z. Wang, H. Liu, M. Le, C. Lin, G. Wu, L. Wang, X. Shi, Y.-G. Jia, *Nat. Commun.* **2023**, *14*, 1331.
- [20] J. Li, J. Cao, B. Lu, G. Gu, *Nat. Rev. Mater.* **2023**, *8*, 604.
- [21] N. Wilkinson, M. Smith, R. Kay, R. Harris, *Int. J. Adv. Manuf. Technol.* **2019**, *105*, 4599.
- [22] E. B. Secor, *Flexible Printed Electron.* **2018**, *3*, 035002.
- [23] D. Zhao, T. Liu, M. Zhang, R. Liang, B. Wang, *Smart Mater. Struct.* **2012**, *21*, 115008.
- [24] a) D. Ratnayake, A. Curry, K. Walsh, presented at 2021 IEEE Int. Conf. on Flexible and Printable Sensors and Systems (FLEPS) 2021, Virtual June 20–23, **2021**; b) S. Li, J. G. Park, S. Wang, R. Liang, C. Zhang, B. Wang, *Carbon* **2014**, *73*, 303.
- [25] A. K. Sinha, G. L. Goh, W. Y. Yeong, Y. Cai, *Adv. Mater. Interfaces* **2022**, *9*, 2200621.
- [26] X. Zhou, L. Zhang, Y. Wang, S. Zhao, Y. Zhou, Y. Guo, Y. Wang, J. Liang, H. Chen, *Adv. Mater. Technol.* **2023**, *8*, 2201272.
- [27] R. R. Salary, J. P. Lombardi III, D. L. Weerawarne, P. K. Rao, M. D. Poliks, presented at Int. Manufacturing Science and Engineering Conf. 2019, Pennsylvania, USA 10–14 June, **2019**.
- [28] Y. Chen, L. Wang, Z. Wu, J. Luo, B. Li, X. Huang, H. Xue, J. Gao, *Composites, Part B* **2019**, *176*, 107358.
- [29] J. Xu, H. Wang, T. Ma, Y. Wu, R. Xue, H. Cui, X. Wu, Y. Wang, X. Huang, W. Yao, *Carbon* **2020**, *166*, 316.
- [30] A. Mehmood, N. Mubarak, M. Khalid, R. Walvekar, E. Abdullah, M. Siddiqui, H. A. Baloch, S. Nizamuddin, S. Mazari, *J. Environ. Chem. Eng.* **2020**, *8*, 103743.
- [31] I. Kim, K. Woo, Z. Zhong, P. Ko, Y. Jang, M. Jung, J. Jo, S. Kwon, S.-H. Lee, S. Lee, *Nanoscale* **2018**, *10*, 7890.
- [32] Y. Ding, J. Yang, C. R. Tolle, Z. Zhu, *ACS Appl. Mater. Interfaces* **2018**, *10*, 16077.
- [33] J. Chen, J. Zhang, Z. Luo, J. Zhang, L. Li, Y. Su, X. Gao, Y. Li, W. Tang, C. Cao, *ACS Appl. Mater. Interfaces* **2020**, *12*, 22200.
- [34] S. M. Khan, J. M. Nassar, M. M. Hussain, *ACS Appl. Electron. Mater.* **2020**, *3*, 30.
- [35] Y.-D. Chen, V. Nagarajan, D. W. Rosen, W. Yu, S. Y. Huang, *J. Manuf. Processes* **2020**, *58*, 55.
- [36] a) D. Tobjörk, R. Österbacka, *Adv. Mater.* **2011**, *23*, 1935; b) Y. Zhang, L. Zhang, K. Cui, S. Ge, X. Cheng, M. Yan, J. Yu, H. Liu, *Adv. Mater.* **2018**, *30*, 1801588.
- [37] S. Chen, Y. Song, D. Ding, Z. Ling, F. Xu, *Adv. Funct. Mater.* **2018**, *28*, 1802547.
- [38] A. Pal, D. Goswami, R. V. Martinez, *Adv. Funct. Mater.* **2020**, *30*, 1906603.
- [39] N. Colozza, V. Caratelli, D. Moscone, F. Arduini, *Biosensors* **2021**, *11*, 328.
- [40] S. K. Mahadeva, K. Walus, B. Stoeber, *ACS Appl. Mater. Interfaces* **2015**, *7*, 8345.
- [41] X. Liao, Q. Liao, X. Yan, Q. Liang, H. Si, M. Li, H. Wu, S. Cao, Y. Zhang, *Adv. Funct. Mater.* **2015**, *25*, 2395.
- [42] Y. Li, Y. A. Samad, T. Taha, G. Cai, S.-Y. Fu, K. Liao, *ACS Sustainable Chem. Eng.* **2016**, *4*, 4288.
- [43] G. J. N. Wang, A. Gasperini, Z. Bao, *Adv. Electron. Mater.* **2018**, *4*, 1700429.
- [44] a) J. Ryu, M. Mohammadifar, M. Tahernia, H. i. Chun, Y. Gao, S. Choi, *Adv. Mater. Technol.* **2020**, *5*, 1901054; b) M. A. C. Angeli, M. Ciocca, L. Petti, P. Lugli, *Advances in Chemical Engineering*, Vol. 57, Academic Press, Massachusetts, USA **2021**, p. 45.
- [45] X.-Y. Guo, W.-B. Li, Q.-H. Gao, H. Yan, Y.-Q. Fei, W.-M. Zhang, *Smart Mater. Struct.* **2020**, *29*, 035033.
- [46] a) R. V. Martinez, C. R. Fish, X. Chen, G. M. Whitesides, *Adv. Funct. Mater.* **2012**, *22*, 1376. b) M. Dou, D. C. Dominguez, X. Li, J. Sanchez, G. Scott, *Anal. Chem.* **2014**, *86*, 7978.
- [47] a) M. Prambauer, C. Paulik, C. Burgstaller, *Composites, Part A* **2015**, *74*, 107; b) M. Amjadi, M. Sitti, *ACS Nano* **2016**, *10*, 10202.
- [48] M. Amjadi, M. Sitti, *Adv. Sci.* **2018**, *5*, 1800239.
- [49] a) P. Zhou, L. Chen, L. Yao, M. Weng, W. Zhang, *Nanoscale* **2018**, *10*, 8422; b) Y. Hu, A. Xu, J. Liu, L. Yang, L. Chang, M. Huang, W. Gu, G. Wu, P. Lu, W. Chen, *Adv. Mater. Technol.* **2019**, *4*, 1800674.
- [50] a) A. del Bosque, X. F. Sánchez-Romate, D. Patrizi, J. S. del Río Sáez, D.-Y. Wang, M. Sánchez, A. Ureña, *Sens. Actuators, A* **2023**, *358*, 114448; b) A. del Bosque, X. F. Sánchez-Romate, A. Gómez, M. Sánchez, A. Ureña, *Sens. Actuators, A* **2023**, *353*, 114249.

- [51] G. Tarabella, D. Vurro, S. Lai, P. D'Angelo, L. Ascari, S. Iannotta, *Flexible Printed Electron.* **2020**, *5*, 014005.
- [52] P. Zhao, Z. Ye, M. Xu, L. Yang, *Advanced Graphic Communication, Printing and Packaging Technology*, Springer, Singapore **2020**.
- [53] E. B. Secor, *Flexible Printed Electron.* **2018**, *3*, 035007.
- [54] R. R. Tafoya, E. B. Secor, *Flexible Printed Electron.* **2020**, *5*, 015009.
- [55] a) N. J. Wilkinson, R. W. Kay, R. A. Harris, *Adv. Mater. Technol.* **2020**, *5*, 2000148; b) A. J. Capel, M. A. Smith, S. Taccola, M. Pardo-Figuerez, R. P. Rimington, M. P. Lewis, S. D. Christie, R. W. Kay, R. A. Harris, *Front. Cell Dev. Biol.* **2021**, *9*, 2347; c) M. A. Smith, N. R. Fry, R. W. Kay, R. A. Harris, presented at 2018 Int. Solid Freeform Fabrication Symp. 2018, Texas, USA August 13–15, **2018**.
- [56] N. J. Wilkinson, M. Lukic-Mann, M. P. Shuttleworth, R. W. Kay, R. A. Harris, presented at 2019 2nd IEEE Int. Conf. on Soft Robotics (RoboSoft), Seoul, South Korea 14–18 April, **2019**.
- [57] M. Serpelloni, E. Cantù, M. Borghetti, E. Sardini, *Sensors* **2020**, *20*, 841.
- [58] N. Attard-Montalto, J. J. Ojeda, A. Reynolds, M. Ismail, M. Bailey, L. Doodkorte, M. De Puit, B. J. Jones, *Analyst* **2014**, *139*, 4641.
- [59] H. J. Cho, N. B. Lu, M. P. Howard, R. A. Adams, S. S. Datta, *Soft Matter* **2019**, *15*, 4689.
- [60] a) N. Dalal, Y. Gu, D. R. Hines, A. Dasgupta, S. Das, *J. Micromech. Microeng.* **2019**, *29*, 097001; b) Z. Chen, W. Pan, D. Yao, M. Gao, Y. Gao, X. Chen, J. Krzywanski, F. Wang, *Colloids Surf. A* **2022**, *650*, 129283; c) J. Brennenman, D. Z. Tansel, G. K. Fedder, R. Panat, *Adv. Mater. Technol.* **2022**, *7*, 2200396.
- [61] S. Liu, Y. Li, S. Xing, L. Liu, G. Zou, P. Zhang, *Materials* **2019**, *12*, 1559.
- [62] J. Thiery, E. Keita, S. Rodts, D. Courtier Murias, T. Kodger, A. Pegoraro, P. Coussot, *Eur. Phys. J. E* **2016**, *39*, 1.
- [63] V. Sanchez-Romaguera, S. Wünscher, B. M. Turki, R. Abbel, S. Barbosa, D. J. Tate, D. Oyeka, J. C. Batchelor, E. A. Parker, U. S. Schubert, *J. Mater. Chem. C* **2015**, *3*, 2132.
- [64] M. Schneider, J. Maurath, S. B. Fischer, M. Weiß, N. Willenbacher, E. Koos, *ACS Appl. Mater. Interfaces* **2017**, *9*, 11095.
- [65] Y. Kwon, C. Park, J. Kim, H. Kim, C. Park, B. Lee, Y. Jeong, S. J. Cho, *Smart Mater. Struct.* **2020**, *29*, 115007.
- [66] Y. Xiao, S. Jiang, Y. Li, W. Zhang, *Smart Mater. Struct.* **2020**, *29*, 045023.
- [67] D. Kang, P. V. Pikhitsa, Y. W. Choi, C. Lee, S. S. Shin, L. Piao, B. Park, K.-Y. Suh, T.-i. Kim, M. Choi, *Nature* **2014**, *516*, 222.
- [68] J. Q. Feng, A. Ramm, M. J. Renn, *Flexible Printed Electron.* **2021**, *6*, 045006.
- [69] R. R. Tafoya, A. W. Cook, B. Kaeher, J. R. Downing, M. C. Hersam, E. B. Secor, *Adv. Mater. Technol.* **2020**, *5*, 2000781.
- [70] D. J. Lee, J. H. Oh, H. S. Bae, *Mater. Lett.* **2010**, *64*, 1069.
- [71] a) T. Schotzko, W. Lang, *Sensors* **2014**, *14*, 12387; b) A. Oliveri, M. Maselli, M. Lodi, M. Storace, M. Cianchetti, *IEEE Trans. Ind. Electron.* **2018**, *66*, 8205.
- [72] S. Schwebke, S. Winter, M. Koch, G. Schultes, *J. Appl. Phys.* **2018**, *124*, 235308.
- [73] Q. Li, H. Liu, S. Zhang, D. Zhang, X. Liu, Y. He, L. Mi, J. Zhang, C. Liu, C. Shen, *ACS Appl. Mater. Interfaces* **2019**, *11*, 21904.
- [74] a) B. Kulyk, B. F. Silva, A. F. Carvalho, S. Silvestre, A. J. Fernandes, R. Martins, E. Fortunato, F. M. Costa, *ACS Appl. Mater. Interfaces* **2021**, *13*, 10210; b) D.-J. Lee, D. Y. Kim, *IEEE Access* **2019**, *7*, 77200.
- [75] Z. Zhang, G. Chen, Y. Xue, Q. Duan, X. Liang, T. Lin, Z. Wu, Y. Tan, Q. Zhao, W. Zheng, *Adv. Funct. Mater.* **2023**, *33*, 2305705.
- [76] D.-S. Kim, Y. W. Choi, A. Shanmugasundaram, Y.-J. Jeong, J. Park, N.-E. Oyunbaatar, E.-S. Kim, M. Choi, D.-W. Lee, *Nat. Commun.* **2020**, *11*, 535.
- [77] Y. Zhou, H. Lian, Z. Li, L. Yin, Q. Ji, K. Li, F. Qi, Y. Huang, *View* **2022**, *3*, 20220025.
- [78] S. K. Hong, S. Yang, S. J. Cho, H. Jeon, G. Lim, *Sensors* **2018**, *18*, 1171.
- [79] a) J. Zhou, H. Yu, X. Xu, F. Han, G. Lubineau, *ACS Appl. Mater. Interfaces* **2017**, *9*, 4835; b) Y. Xin, J. Zhou, X. Xu, G. Lubineau, *Nanoscale* **2017**, *9*, 10897.
- [80] B. Mosadegh, P. Polygerinos, C. Keplinger, S. Wennstedt, R. F. Shepherd, U. Gupta, J. Shim, K. Bertoldi, C. J. Walsh, G. M. Whitesides, *Adv. Funct. Mater.* **2014**, *24*, 2163.